Crustal inheritance and a top-down control on arc magmatism at Mount St. Helens

Paul A. Bedrosian[1]*, Jared R. Peacock[2], Esteban Bowles-Martinez[3], Adam Schultz[3], Graham J. Hill[4]

[1]United States Geological Survey, Denver, CO, USA

[2]United States Geological Survey, Menlo Park, CA, USA

[3]Oregon State University, Corvallis, OR, USA

[4]University of Canterbury, Gateway Antarctica, Christchurch, NZ

*e-mail: pbedrosian@usgs.gov

In a subduction zone, the volcanic arc marks the location where magma, generated via flux melting in the mantle wedge, migrates through the crust and erupts. While the location of deep magma broadly defines the arc position, here we argue that crustal structures, identified in geophysical data from the Washington Cascades magmatic arc, are equally important in controlling magma ascent and defining the spatial distribution and compositional variability of erupted material. As imaged by a three-dimensional resistivity model, a broad lower-crustal mush zone containing 3-10% interconnected melt underlies this segment of the arc, interpreted to episodically feed upper-crustal magmatic systems and drive eruptions. Mount St. Helens is fed by melt channeled around a mid-Tertiary batholith also imaged in the resistivity model and supported by potential-field data. Regionally, volcanism and seismicity are almost exclusive of the batholith, while at Mount St. Helens, along its margin, the ascent of viscous felsic melt is enabled by deep-seated metasedimentary rocks. Both the anomalous forearc location and

composition of St. Helens magmas are products of this zone of localized extension along the batholith margin. This work is a compelling example of inherited structural control on local stress state and magmatism.

Structure and evolution of the Washington Cascades

The Cascades magmatic arc includes ~2,300 Quaternary vents spread over 1,250 kilometers[1], the result of subduction of the Juan de Fuca plate beneath North America (Fig. 1, inset). The arc segment between Mount Rainier and Mount Hood is anomalous in that significant forearc and backarc volcanism occurs with no attendant complexity in slab geometry[2]. Mount Rainier (MR), Indian Heaven (IH), and Mount St. Helens (MSH) are all located tens of kilometers west of the main andesitic arc. MSH, the most active volcano in the entire arc, is petrologically distinct, erupting almost exclusively dacite, reflecting a greater degree of differentiation than andesitic vents along the main arc. Compositional heterogeneity of the forearc is also evidenced by the monogenetic IH volcanic field and the Boring volcanic field[1].

In southern Washington the magmatic arc overprints a poorly exposed suture formed by the accretion of the Siletz large igneous province to Mesozoic North America in the Eocene[3,4]. The suture is marked by sedimentary rocks, the oldest being marine sediments deposited at the time of accretion. Subduction began off the western edge of Siletzia by 45 Ma, interbedding volcanic rocks erupted from the ancestral Cascades arc and continental sedimentary rocks. A mid-Tertiary plate reorganization (approximately) marks the onset of forearc rotation[5], initiating intrusion of intermediate to felsic plutons (e.g. Snoqualmie batholith north of our study area) along a belt stretching from the Columbia River to Glacier Peak[6]. The southern Washington segment of the modern arc is located at a transition between convergence, basement uplift, and sparse volcanism to the north and extension and widespread volcanism to the south. This region overlaps with the Southern Washington crustal conductor (SWCC), an enigmatic conductivity anomaly that has alternately been attributed to metasedimentary rocks[7] and lower-crustal melt[8]. These divergent explanations have markedly different implications for volcanic hazards and regional tectonics.

Anomalous electrical conductivity in the southern Washington Cascades was first identified from magnetovariational data that suggested a north-south trending crustal conductor[9]. 2D resistivity models derived from magnetotelluric (MT) data defined the SWCC as a dipping conductor (>2 S/m) extending into the lower crust, with high conductivity attributed to forearc basin sediments accreted against the Mesozoic North American margin[7]. Later studies refined the geometry of the SWCC to lie between MSH, MR and Mount Adams (MA) (Extended Data Fig. 1), and suggested its influence on crustal deformation and volcanism[10]. A focused 3D investigation of the MSH area imaged a strong conductor (10 S/m) at 3-12 km depth[8], attributed to an upper-crustal magma chamber in accordance with seismic and petrologic studies[11]. Moreover, 2D modeling along a profile from MSH to MA imaged the SWCC as a lower-crustal conductor interpreted as a mush zone with 2-12% interconnected melt potentially feeding multiple volcanic systems. Reconciling these opposing interpretations of the SWCC is a goal of the current study. Prior MT investigations were limited by survey aperture, data density, or by 1D and 2D modeling assumptions. Our work is based upon 3D inverse modeling of new, high-density MT data covering the full extent of the SWCC together with preexisting data (Extended Data Fig. 1)[8,12-13]. The methods summary describes new data collection, processing, and inversion as well as an assessment of our model in relation to previous studies.

Regional resistivity structure

The 3D resistivity model images sub-vertical belts of extremely high conductivity (> 1 S/m) within an otherwise resistive upper-crustal column (Fig. 1,2a). These conductive belts span much of the model area, and are evident within the measured data as abrupt spatial changes in both induction vectors and phase tensors (Extended Data Fig. 2). The narrow conductive belts extend in places to the near-surface and in the north correlate with Eocene sedimentary rocks, specifically exposures of carbonaceous shale within regional anticlines (Fig. 1)[7]. The conductive belts continue south to 46°N, beyond the southernmost exposure of Eocene rocks (Fig. 2a). The western extent of high conductivity coincides with the Mount St. Helens and West Rainier seismic zones (MSZ, WRSZ) and mimics the eastern edge of the Siletz terrane (Fig. 2a), interpreted from potential-field[14-15] and seismic data[16-17] to lie to the west of MR and beneath or slightly west of MSH. Resistive areas coincide with mapped or inferred Miocene intrusive rocks (Fig. 1)[6,18]. With few exceptions, high resistivity correlates with plutonic rocks and high conductivity with metasedimentary rocks.

The near-surface conductive belts coalesce into a ring structure at greater depth, outlining a 2,000 km^2 ovoid resistor (Fig. 2a). The northwest corner of the resistor includes the exposed Spirit Lake pluton[6], interpreted to be part of a much larger plutonic complex than previously recognized, herein called the Spirit Lake Batholith (SLB). Magnetic potential data (Fig. 2b), which reflect contrasts in magnetization, reveal a coincident potential high correlated with exposed intrusive rocks, and potential lows correlated with high conductivity belts. In greater detail, the magnetic potential data reveal a ‘divot’ removed from the southern margin of the SLB that correlates to both a reduction in resistivity and the northern extent of the IH volcanic field. The potential high over the SLB is consistent with moderate magnetic susceptibilities expected for the Spirit Lake granodiorite, while potential lows are conforming with low-susceptibility metasedimentary rocks[7]. These correlations continue north of the ring structure for at least 40 km, where high conductivity follows the Carbon River anticline (CRA), wedged between the resistive Tatoosh pluton to the east and unnamed Miocene intrusive rocks to the west.

Graphite, created via contact metamorphism[6], and/or metallic sulfides, resulting from mineralization adjacent to the Spirit Lake pluton[19], provide a logical explanation for the high conductivity, the ring-shaped geometry and the absence of similar conductive belts elsewhere along the Siletz margin[20]. An exceptionally wide contact-metamorphic aureole, between 1.5 and 4 km across[7] and with an inner zone of amphibole hornfels, surrounds the Spirit Lake pluton. Both the Eocene source rocks (carbonaceous marine shales) and the local metamorphic grade (amphibolite facies) are consistent with graphite formation. Metallic sulfides, precipitated via the interaction of magmatic brines exsolved from the SLB with sulfur-rich gases liberated from deep mafic magmas[21], provide an equally viable explanation.

The upper-crustal resistivity structure reflects the region's tectonic history. In contrast, lower-crustal structure (24 km depth; Fig. 3) reflects modern subduction-zone processes. Moderately resistive lower crust is imaged beneath the Siletz forearc and Mesozoic backarc, however a 40-60 km wide conductive zone lies between (dashed lines, Fig. 3), part of a larger feature extending beneath much of the Cascades arc[22]. The position of this lower-crustal conductor (LCC), centered ~25 km seaward of the arc, is accordant with global observations of LCCs in subduction zones[23-24]. The western boundary of the LCC is remarkably similar to the eastern edge of the Siletz terrane (white dashed line, Fig. 2). Along-strike variations in the conductivity of the LCC reflect differing degrees of screening from overlying conductors and are not required by the data.

Examining the LCC in terms of depth-integrated conductivity, or conductance (Extended Data Fig. 3), reveals the compound nature of the SWCC. Conductance of the upper-crustal conductor (UCC) exceeds that of the LCC by an order of magnitude. The UCC is confined to the brittle upper crust and the LCC to the ductile lower crust, separated from one another by a region of moderate resistivity. The transition occurs at depths of 15-20 km, with distinct spatial extents for the upper- and lower-crustal conductance plots (Extended Data Fig. 3). Previous 2D modeling[8] imaged a 1-10 Ω·m conductive path between the UCC and LCC (Extended Data Fig. 4a), particularly west of MA. This apparent connection is a direct consequence of modeling a 3D structure (Fig. 2a) in 2D.

The ability of the iMUSH station array to image the geometry of the UCC and LCC is demonstrated through a synthetic inversion study (Extended Data Fig. 5), details of which are described in the Methods Summary. Additional depth slices through the resistivity model at 1.5, 4. 15, and 36 km are included in Extended Data Fig. 6.

Inherited structural control on magmatism

Constraints on the resistivity of the LCC are critical to its interpretation, hence we varied lower-crustal (20-40 km) resistivity in a forward modeling study and examined the subsequent data misfits (Extended Data Fig. 7). The best constraints come from beneath the resistive SLB, where screening effects are minimal; a resistivity of 5-15 Ω·m is found to be most consistent with the data. Given this constraint, we estimate the LCC could be produced by 3-10% interconnected dacitic melt, assuming petrologic estimates for lower-crust melt feeding MSH (65% SiO_2, 7 wt % water, 5 wt % Na_2O, 950°C, 700 MPa)[25-26]. Decreased water content or increased pressure increase the required melt fraction, whereas increased temperature or a more mafic melt composition reduce it. There is likely some contribution to the LCC from free aqueous fluids, however a water-only model is unlikely given petrologic studies, both locally[25,27] and globally[28], suggesting long-lived lower-crustal mush zones in continental-arc environments. The LCC encompasses a previously imaged deep conductor[8] (Extended Data Fig. 4a) and overlaps partially with a low-velocity zone at similar depth[29]; anomalies in both studies were attributed to melt, with melt fractions comparable to our estimate. Our model indicates that the LCC is separated from the UCC by a region of ~100 Ω·m resistivity (Extended Data Fig. 4b). Given the above petrologic estimates, this region is effectively dry, containing at most 0.5% melt; we speculate that only during episodic recharge does this region contain melt.

Our 3D model bears similarities and differences to previous studies. A conductor beneath MSH, previously interpreted in terms of shallow magma storage[8], is coincident with a conductor in our model (Extended Data Fig. 4). Our model, however, images this conductor extending tens of kilometers from the volcano as part of the western metasedimentary belt surrounding the SLB (Fig. 2a). While conductivity enhancement due to melt (pure melt conductivity ~1 S/m) may contribute to this conductor, it is dwarfed by the conductivity of the metasedimentary rocks (~10 S/m). Thus, while multiple lines of evidence point to shallow magma storage beneath MSH[11], a focused magmatic system cannot be distinguished from the regional metasedimentary belt on the basis of conductivity. A similar scenario exists northwest of MR, where 2D modeling interpreted an upper-crustal conductor in terms of melt[12], while our 3D model images this conductor as part of a 50-km long conductive belt following the CRA and WRSZ (Fig. 1). A cross-section through MR (Extended Data Fig. 8a) reveals no connection between the conductor and either seismicity beneath the edifice (a reflection of shallow magmatic processes) or deep long-period earthquakes (suggestive of fluid or melt transport)[30,31].

Relating our 3D model to volcanism, Quaternary vents and seismicity are sparse within or above the SLB (Fig. 2). The exception is basaltic vents at IH, which erupt across the thin southern margin of the SLB. More striking is the alignment of the admittedly few felsic (dacite) vents with interpreted metasedimentary belts. This includes the area around MSH, dacite erupted at MR above a basal syncline of Eocene rocks[32] and an isolated dacite dome to the west of MR atop the CRA (Fig. 2, Extended Data Fig. 8).

The non-uniform vent distribution and petrologic variability is in contrast to the interpreted lower-crustal mush zone, imaged as a broad arc-parallel swath, bulging westward into the forearc near MSH. Nearly all Quaternary vents fall within the spatial extent of the LCC, with the main arc falling near its eastern margin (Fig. 3), IH within its center, and the limited number of dacite vents near the periphery. We conclude that the brittle upper crust acts as a 'magmatic filter,' modifying the ascent pathways for deep-crustal melt. The SLB appears to inhibit melt ascent, whereas deep-seated bands of metasedimentary rock, particularly where correlated with deformation and seismicity, enable the ascent of viscous dacite melt.

Why is erupted dacite spatially restricted despite being formed deep in the crust[25,27] within a broad evolving mush zone? Why too the sparsity of volcanism above the SLB and neighboring plutons? The expected density contrast between granodiorite of the SLB and adjacent metasedimentary rock is expected to be slight. If anything, the latter may be less dense, which would favor buoyant ascent within the SLB. Thus, density variations are not expected to cause the observed vent distribution and compositional 'focusing.'

We look to large silicic systems, the source of most dacite and rhyolite in compressional arcs, as an analogy. Globally, these systems are correlated with high plate-convergence rates, localized zones of extension, and pre-existing structures[33]. A study of silicic systems in extensional environments further highlights the control of pre-existing structures on the location and orientation of deep-crustal magmatism, and the importance of the local stress regime on faulting and shallow magmatism[34].

Without the high magma flux typical of caldera systems and without sufficient buoyancy to propel these melts to the surface, we conclude that at MSH, pre-existing structures are essential to the ascent and eruption of small batches of dacite melt. Magma overpressure, able to overcome viscous drag and drive vertical diking in the brittle crust, is taken to be more efficient within deep-seated, fractured metasedimentary rock than within the less vertically connected SLB (Fig. 4). Additionally, both the MSZ and the WRSZ are likely localized zones of extension[35], where magma pressure overcomes the minimum horizontal stress and ascends; in contrast, within the SLB and neighboring plutons, magma stalls at mid-crustal levels where horizontal stress is more typical of the overall compressional regime.

Our model illustrates the control that inherited structures, specifically a crustal suture and the plutons that intrude it, have on magmatism (Fig. 4, Supplementary Material). Melts segregated from a lower-crustal mush zone episodically ascend and erupt through this crustal filter, producing the observed vent distribution. In the Washington Cascades, felsic vents are almost exclusively situated above belts of deep-seated metasedimentary rock (and notably absent elsewhere) that broadly define the geometry of the deep mush zone. MSH, located 60 km east of the main volcanic arc along the MSZ, sits directly atop one such belt in a localized extensional environment along the edge of the SLB. To the north, the WRSZ tracks a similar metasedimentary belt. Both belts are the loci for deep, long-period earthquakes taken to reflect episodic melt ascent from the edges of the deep mush zone into the upper-crustal plumbing systems that feeds MSH and MR. Thus the location of the most silicic systems, the source of highly explosive eruptions, may be defined by the intersection of crustal faults or sutures with lower-crustal mush zones.

References

[1]Hildreth, W., Quaternary magmatism in the Cascades – geologic perspectives. *U.S. Geological Survey Professional Paper* **1744**, (2007).

[2]Blair, J.L., McCrory, P.A., Oppenheimer, D.H. & Waldhauser, F. A geo-referenced 3D model of the Juan de Fuca slab and associated seismicity. *U.S. Geological Survey Data Series* **633**, (2013).

[3]Snavely, P.D., Jr. Tertiary geologic framework, neotectonics, and petroleum potential of the Oregon-Washington continental margin. in Scholl, et al., eds., Geology and resource potential of the continental margin of western North America and adjacent ocean basins–Beaufort Sea to Baja California: Circum-Pacific Council for Energy and Mineral Resources Earth Science Series **6**, 305–335 (1987).

[4]Wells, R., Bukry, D., Friedman, R., Pyle, D., Duncan, R., Haeussler, P. & Wooden, J. Geologic history of Siletzia, a large igneous province in the Oregon and Washington Coast Range: Correlation to the geomagnetic polarity time scale and implications for a long-lived Yellowstone hotspot. *Geosphere* **10**, 692–719 (2014).

[5]Wells, R.E. & McCaffrey, R. Steady rotation of the Cascade arc. *Geology* **41**, 1027–1030 (2013).

[6]Evarts, R.C., Ashley, R.P. & Smith, J.G. Geology of the Mount St. Helens Area: Record of Discontinuous Volcanic and Plutonic Activity in the Cascade Arc of Southern Washington. *J. Geophys. Res.* **92**, 10,155–10,169 (1987).

[7]Stanley, W.D., Finn, C. & Plesha, J.L. Tectonics and conductivity structure in the Southern Washington Cascades. *J. Geophys. Res.* **92**, 10,179–10,193 (1987).

[8]Hill, G.J., Caldwell, T.G., Heise, W., Chertkoff, D.G., Bibby, H.M., Burgess, M.K., Cull, J.P. & Cas, R.A.F. Distribution of melt beneath Mount St Helens and Mount Adams inferred from magnetotelluric data. *Nat. Geosci.* **2**, 785–789 (2009).

[9]Law, L.K., Auld, D.R. & Booker, J.R. A geomagnetic variation anomaly coincident with the Cascade volcanic belt. *J. Geophys. Res.* **85**, 5297–5302 (1980).

[10]Egbert, G.D. & Booker J.R. Imaging crustal structure in Southwestern Washington with small magnetometer arrays. *J. Geophys. Res.* **98**, 15,967–15,985 (1993).

[11]Pallister, J.S., Thornber, C.R., Cashman, K.V., Clynne, M.A., Lowers, H.A., Mandeville, C.W., Brownfield, I.K. & Meeker, G.P. Petrology of the 2004–2006 Mount St. Helens lava dome-implications for magmatic plumbing and eruption triggering. *In:* Sherrod, D.R., Scott, W.E. & Stauffer, P.H. (eds.) A volcano rekindled: the renewed eruption of Mount St. Helens, *U.S. Geological Survey Professional Paper* **1750**, (2008).

[12]McGary, R.S., Evans, R.L., Wannamaker, P.E., Elsenbeck, J. & Rondenay, S. Pathway from subducting slab to surface for melt and fluids beneath Mount Rainier. *Nature* **511**, 338–340 (2014).

[13]Schultz, A., G. D. Egbert, A. Kelbert, T. Peery, V. Clote, B. Fry, S. Erofeeva and staff of the National Geoelectromagnetic Facility and their contractors. USArray TA magnetotelluric transfer functions. doi:10.17611/DP/EMTF/USARRAY/TA. (2006–2018).

[14]Finn, C. Geophysical constraints on convergent margin structure. *J. Geophys. Res.* **95**, 19,533–19,546 (1990).

[15]Wells, R.E., Weaver, C.S. & Blakely, R.J. Forearc migration in Cascadia and its neo tectonic significance. *Geology* **26**, 759–762 (1998).

[16]Parsons, T., Trehu, A.M., Luetgert, J.H., Miller, K., Kilbride, F., Wells, R.E., Fisher, M.A., Flueh, E, ten Brink, U.S. & Christiansen, N.I. A new view into the Cascadia subduction zone and volcanic arc: implications for earthquake hazards along the Washington margin. *Geology* **26**, 199–202 (1998).

[17]Stanley, D., Villasenor, A. & Benz, H. Subduction zone and crustal dynamics of western Washington: A tectonic model for earthquake hazards. *U.S. Geological Survey Open-File Report* **99–311,** (1995).

[18]Williams, D.L. & Finn, C. Evidence for a shallow pluton beneath the Goat Rocks Wilderness, Washington, from gravity and magnetic data. *J. Geophys. Res.* **92**, 4867–4880 (1987).

[19]Iveson, A.A., Webster, J.D., Rowe, M.C. & Neill, O.K. Magmatic–hydrothermal fluids and volatile metals in the Spirit Lake pluton and Margaret Cu–Mo porphyry system, SW Washington, USA. *Contrib. Mineral. Petrol.* **171,** 20 (2016).

[20]Bedrosian, P.A. & Feucht, D.W. Structure and tectonics of the northwestern United States from EarthScope USArray magnetotelluric data. *Earth Planet. Sci. Lett.* **402**, 275–289 (2014).

[21]Blundy, J., Mavrogenes, J., Tattitch, B., Sparks, S. & Gilmer, A. Generation of porphyry copper deposits by gas–brine reaction in volcanic arcs. *Nat. Geosci.* **8**, 235–240 (2015).

[22]Patro, P.K. & Egbert, G.D. Regional conductivity structure of Cascadia: Preliminary results from 3D inversion of USArray transportable array magnetotelluric data. *Geophys. Res. Lett.* **35**, L20311 (2008).

[23]Worzewski, T., Jegen, M., Kopp, H., Brasse, H. & Castillo, W.T. Magnetotelluric image of the fluid cycle in the Costa Rican subduction zone. *Nat. Geosci.* **4**, 108–111 (2010).

[24]Wannamaker, P.E., Evans, R.L., Bedrosian, P.A., Unsworth, M.J., Maris, V. & McGary, R.S. Segmentation of plate coupling, fate of subduction fluids, and modes of arc magmatism in Cascadia, inferred from magnetotelluric resistivity. *Geochem. Geophys. Geosyst.* **15**, 4320–4253 (2014).

[25]Blatter, D.L., Sisson, T.W. & Hankins, W.B. Voluminous arc dacites as amphibole reaction-boundary liquids. *Contrib. Mineral Petrol.* **172**, 27 (2017).

[26]Pommier, A. & Le-Trong E. "SIGMELTS": A web portal for electrical conductivity calculations in geosciences. *Comp. & Geosci.* **37**, 1450–1459 (2011).

[27]Claiborne, L.L., Miller, C.F., Flanagan, D.M., Clynne, M.A. & Wooden, J.L. Zircon reveals protracted magma storage and recycling beneath Mount St. Helens. *Geology,* **38**, 1011–1014 (2010).

[28]Cashman, K.V., Sparks, R.S.J. & Blundy, R.J. Vertically extensive and unstable magmatic systems: A unified view of igneous processes. *Science,* **355**, 1280 (2017).

[29]Flinders, A.F. & Shen, Y. Seismic evidence for a possible deep crustal hot zone beneath Southwest Washington. *Nat. Sci. Rpt.* **7**, 7400 (2017).

[30]Nichols, M. L., Malone, S. D., Moran, S. C., Thelen, W. A. & Vidale, J. E. Deep long-period earthquakes beneath Washington and Oregon volcanoes. *J. Volcanol. Geotherm. Res.* **200**, 116–128 (2011).

[31]Kiser, E., Palomeras, I., Levander, A., Zelt, C., Harder, S., Schmandt, B., Hansen, S., Creager, K. & Ulberg, C. Magma reservoirs from the upper crust to the Moho inferred from high-resolution Vp and Vs models beneath Mount St. Helens, Washington State, USA. *Geology,* **44**, 411–416 (2016).

[32]Sisson, T.W., Salters, J.V.M. & Larson, P.B. Petrogenesis of Mount Rainier andesite: Magma flux and geologic controls on the contrasting differentiation styles at stratovolcanoes of the southern Washington Cascades. *Geol. Soc. Amer. Bull.* **126**, 122–144 (2014).

[33]Hughes, G.R. & Mahood, G.A. Silicic calderas in arc settings: Characteristics, distribution, and tectonic controls. *Geol. Soc. Amer. Bull.* **123**, 1577–1595 (2011).

[34]Robertson, E.A.M., Biggs, J., Cashman, K.V., Floyd, M.A. & Vye-Brown, C. Influence of regional tectonics and pre-existing structures on the formation of elliptical calderas in the Kenyan Rift, in: Magmatic Rifting and Active Volcanism, Wright, T,J, Ayele, A., Ferguson, D.J., Kidane, T. & Vye-Brown, C. (eds.). *Geological Society, London Special Publication* **420** (2015).

[35]Weaver, C.S., Grant, W.C. & Shemeta, J.E. Local crustal extension at Mount St. Helens, Washington. *J. Geophys. Res.* **92**, 10,170–10,178 (1987).

Corresponding Author: Paul A. Bedrosian, Geology, Geophysics, and Geochemistry Science Center, United States Geological Survey, Denver Colorado, USA, pbedrosian@usgs.gov

Acknowledgments

We thank A. Adams, L. Ball, B. Bloss, L. Bonner, B. Burton, T. Bye, B. Fry, E. Hart, M. Lee, K. Menoza, and M. Wisniewski for their invaluable contributions to the data collection effort. We thank the Gifford-Pinchot National Forest, Weyerhaeuser, the Washington DNR, Mt. Rainier National Park, Port Blakely Tree Farms, Hancock Forest Resources, Pope Resources, West Fork Timber Company, the White Pass ski area and numerous private landowners for land access without which this work would not have been possible. T. Sisson, C. Finn, Olivier Bachmann, R. Blakely and J. Glen provided valuable discussion and critical input that helped to shape this manuscript. We thank R. Blakely and C. Finn for processing the magnetic field data (available at https://mrdata.usgs.gov/airborne/), R. Evans and Phil Wannamaker for making the Café MT data publicly available (available at https://ds.iris.edu/spud/emtf), and D. Ramsey for providing Quaternary vent locations. Seismicity is from the Pacific Northwest Seismic Network. This research used resources provided by the Core Science Analytics, Synthesis, & Libraries (CSASL) Advanced Research Computing (ARC) group at the U.S. Geological Survey (USGS). This work was supported by the USGS Volcano Hazards and Mineral Resources Programs and the U.S. National Science Foundation grant EAR1144353 through the GeoPrisms program. Any use of trade, firm, or product names is for descriptive purposes only and does not imply endorsement by the U.S. Government.

Author Contributions

The iMUSH MT experiment was conceived by PAB and AS. AS and PAB coordinated and led the data collection effort, with data collection primarily carried out by EBM and JP. Time-series processing of the data was done by PAB, JP and GJH. PAB, JP and EBM carried out the inversion and model development. The interpretation and development of the conceptual model was led by PAB. All authors contributed to the understanding of the results and editing of the manuscript.

Figure 1. Resistivity at 3 km depth with the outline of Miocene intrusive rocks (white) and Eocene sedimentary rocks (black). Profile AA' shown in Figure 4. Carbon River anticline (CRA); Goat Rocks (GR); Goat Rocks pluton (GRP); Indian Heaven (IH); Morton anticline (MoA); Mt. Adams (MA); Mt. Rainier (MR); Mount St. Helens (MSH); Skate Mountain anticline (SMA); Silver Star pluton (SSP); Spirit Lake batholith (SLB); Spirit Lake pluton (SLP); Spud Mountain pluton (SMP); Tatoosh pluton (TP); White Pass anticline (WPA). Thick red line indicates the axis of the volcanic arc and grey box indicates extent of IH vent field. Inset shows Juan de Fuca subduction zone with Cascades arc volcanoes (red) and depth contours[2] in 10-km intervals to the top of the slab. White box indicates study area.

Figure 2. Geophysical expression of the SLB and surrounding metasedimentary belts. (a) Resistivity at 7 km depth with interpreted eastern edge of the Siletz terrane (white dashed line), exposed extent of Mesozoic rocks (pink outline), seismicity (black dots), Quaternary dacite vents (white circles) and other Quaternary vents (pink circles). (b) Magnetic potential for same region. Abbreviations as in Figure 1 plus Mount St. Helens seismic zone (MSZ); West Rainier seismic zone (WRSZ). Deep long-period earthquakes[34] shown as green stars.

Figure 3. Resistivity at 24 km depth with seismicity (black dots), Quaternary dacite vents (white circles), other Quaternary vents (pink circles), and deep long-period earthquakes[34] (green stars). Approximate extent of lower-crustal conductor denoted by black dashed lines. Abbreviations as in Figure 1.

Figure 4. Perspective view through the 3D resistivity model and interpreted crustal architecture. Isosurfaces are at resistivity greater than 300 Ω·m (blue) and less than 10 Ω·m (orange). Lower-crustal conductivity is attributed to a mush zone containing 3-10% melt and exsolved magmatic fluids. Fluids and melt preferentially ascend along steeply-dipping belts of metasedimentary rock and around the SLB and neighboring plutons. These belts are the locus of seismicity along the MSZ and WRSZ. Vents erupting dacite are almost exclusively located above these belts. The location of profile A-A' is shown in Figure 1. Seismicity shown in black; deep long-period earthquakes in white[34]. Abbreviations as in Figure 1 plus Juan de Fuca (JdF); lower-crustal conductor (LCC); Mesozoic North America (MzNA); Siletz terrane (ST). σ_3 denotes interpreted minimum principal stress direction.

Methods Summary

As part of the imaging Magma Under St. Helens (iMUSH) project, we collected 145 wideband MT stations (Extended Data Fig. 1) with a nominal station spacing of 7 km and a period range of 0.01-1000 s. The newly collected MT data were combined with a dense array of stations surrounding MSH[8], a profile north of MR from the Café MT study[12], regional EarthScope stations[12], and unpublished data from ongoing investigations into forearc structure and geothermal investigations near MSH. Both full impedance data and vertical magnetic-field transfer functions (tippers) were inverted for the combined 295-site data set in 3D using the modular inversion code ModEM[36-37]. Data were inverted at 23 frequencies from 300 to 0.001 Hz using a mesh with a uniform 1 km horizontal cell size and a non-uniform vertical mesh with a surface cell thickness of 20 m. The model contains over 1.5 million model cells. Data were inverted with statistically-determined errors, subject to defined error floors. A sequential inversion approach was used to balance the fit between impedance and tipper data and to progressively build structure within the model while simultaneously reducing error floors (Extended Data Fig. 9). A final data misfit of 2.24 was obtained, which represents an 88% reduction in misfit relative to the starting halfspace model (Extended Data Fig. 10). Examination of data misfit by frequency, site, and component reveals a relatively white fit, with no systematic patterns in misfit.

A synthetic inversion study (Extended Data Fig. 5) was carried out to demonstrate the ability to recover the geometry and amplitude of the UCC and LCC. We model the UCC as a 5-km wide ring conductor (1 Ω·m) extending from 1 to 16 km depth within a resistive 1000 Ω·m host. The LCC is modeled as a 10 Ω·m conductive zone extending along the axis of the magmatic arc, from 40-60 km wide and from 20-40 km depth. Synthetic data were generated from these models at the same stations and period range as the measured data. Gaussian noise was applied to the synthetic data prior to inversion and applied data errors are equivalent to the error floors applied to the measured data. The sequential inversion approach applied to the measured data (Extended Data Fig. 9) was used for the sequential inversion.

Methods references

[36]Egbert, G.D. & Kelbert, A. Computational recipes for electromagnetic inverse problems. *Geophys. J. Int.* **189**, 251-267 (2012).

[37]Kelbert, A. Meqbel, N., Egbert, G.D. & Tandon, K. ModEM: a modular system for inversion of electromagnetic geophysical data. *Comput. Geosci.* **66**, 40-53 (2014).

Data availability

The magnetic field data are available at https://mrdata.usgs.gov/airborne/, the Earthscope and Café MT data are available at https://ds.iris.edu/spud/emtf, and the resistivity model presented here can be visualized or downloaded at the IRIS Earth Model Collaboration (https://ds.iris.edu/ds/products/emc-earthmodels/). The iMUSH MT data are planned to be released later this year on ScienceBase at https://doi.org/doi:10.5066/P9NLXXB3: in the meantime the data that support the findings of this study are available from the corresponding author upon request.

Code availability

The ModEM code used to generate the 3D resistivity model is available for non-commercial research purposes and can be accessed at http://www.modem-geophysics.com.

Supplementary material

Movie. 3D rendering of the resistivity model. Upper 3 km of model is removed for clarity. Seismicity greater than M=1 shown as grey spheres, long-period earthquakes are in white. Low-resistivity isosurface progressively increases from 3 Ω·m to 20 Ω·m. High-resistivity isosurface progressively decreases from 2000 Ω·m to 300 Ω·m. Goat Rocks (GR); Indian Heavan (IH); lower-crustal conductor (LCC); Mt. Adams (MA); Mt. Rainier (MR); Mount St. Helens (MSH); Mount St. Helens seismic zone (MSZ); Silver Star pluton (SSP); Spirit Lake batholith (SLB); Spirit Lake batholith (SLB); Spud Mountain pluton (SMP); Tatoosh pluton (TP); West Rainier seismic zone (WRSZ).

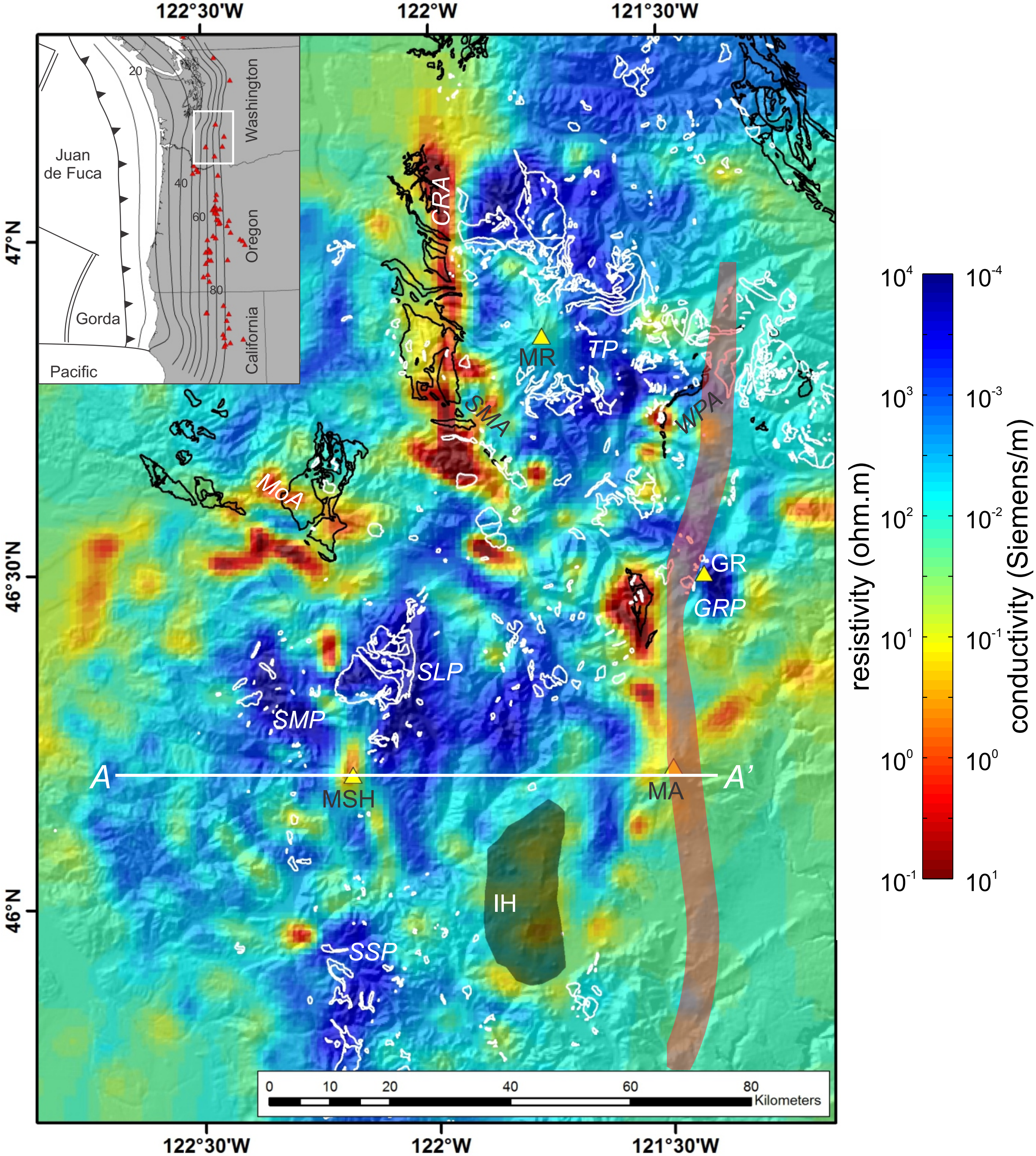
122°30'W
122°W
121°30'W
47°N
46°30'N
46°N
Juan de Fuca
Gorda
Pacific
Washington
Oregon
California
20
40
60
80
CRA
MR
TP
SMA
WPA
MoA
GR
GRP
SLP
SMP
A
A'
MSH
MA
IH
SSP
0
10
20
40
60
80
Kilometers
resistivity (ohm.m)
conductivity (Siemens/m)
10^4
10^3
10^2
10^1
10^0
10^-1
10^-4
10^-3
10^-2
10^-1
10^0
10^1

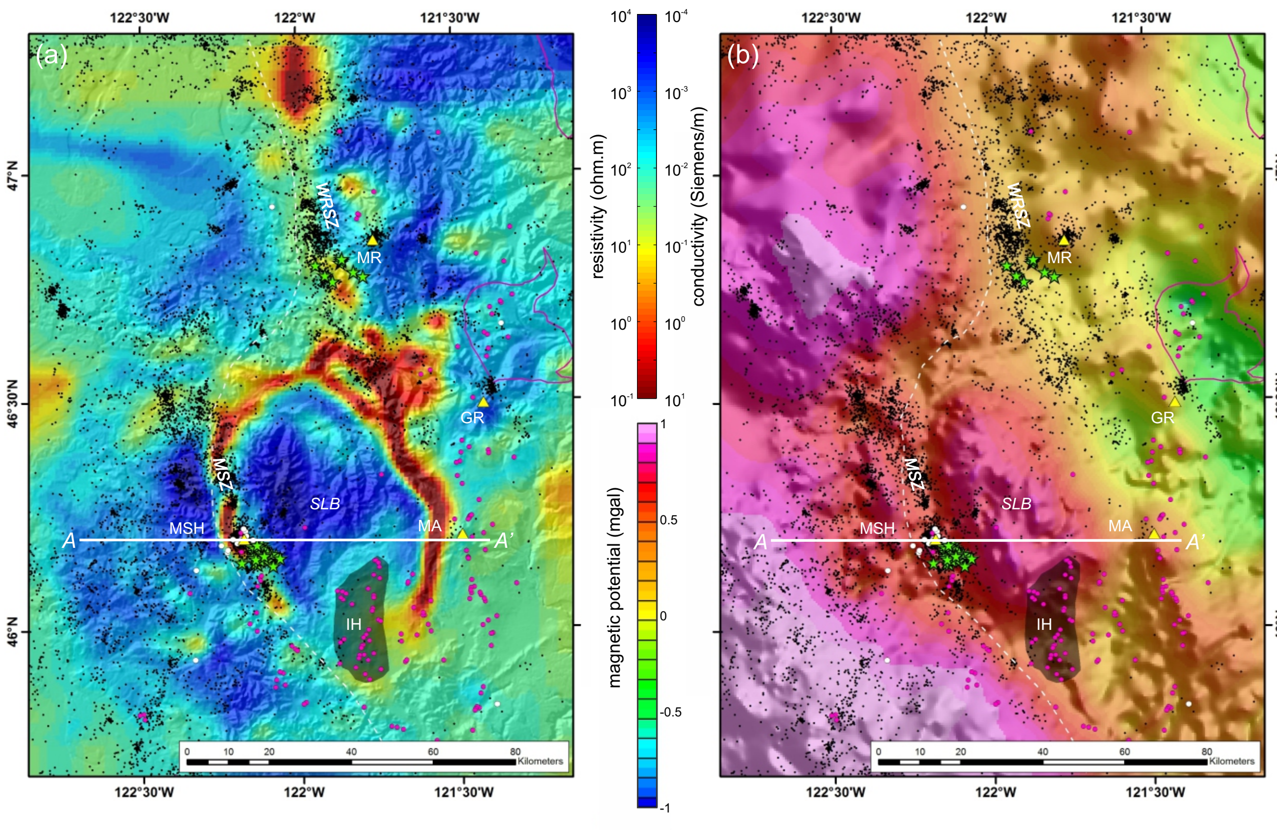

(a)
(b)
122°30'W
122°W
121°30'W
47°N
46°30'N
46°N
WRSZ
MR
GR
MSZ
SLB
MSH
MA
A
A'
IH
Kilometers
resistivity (ohm.m)
conductivity (Siemens/m)
magnetic potential (mgal)

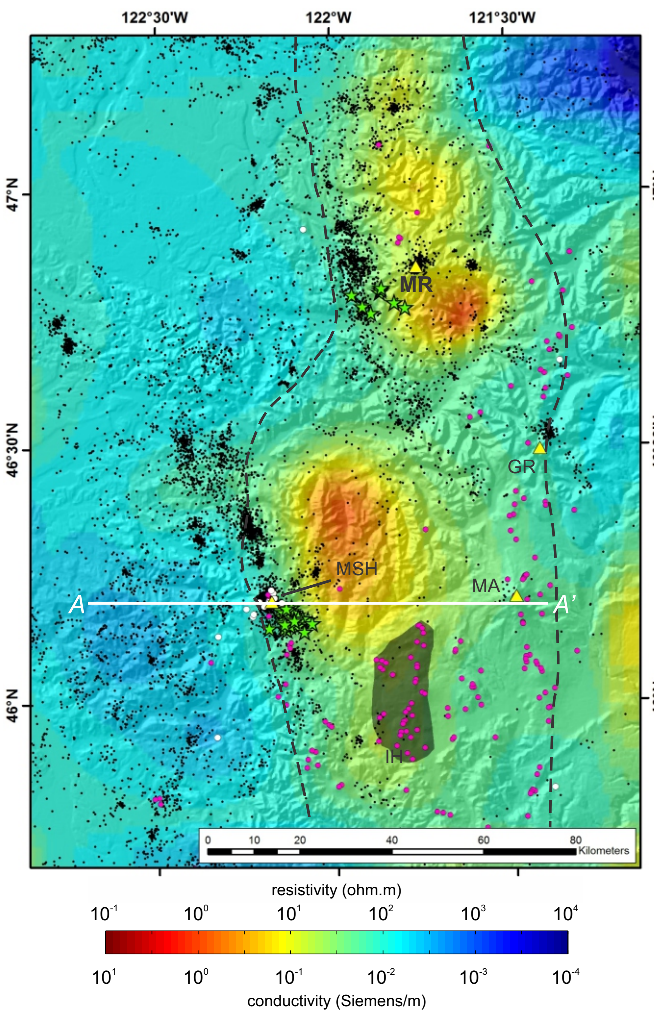
122°30'W
122°W
121°30'W
47°N
46°30'N
46°N
MR
GR
MSH
MA
A
A'
IH
0
10
20
40
60
80
Kilometers
resistivity (ohm.m)
conductivity (Siemens/m)

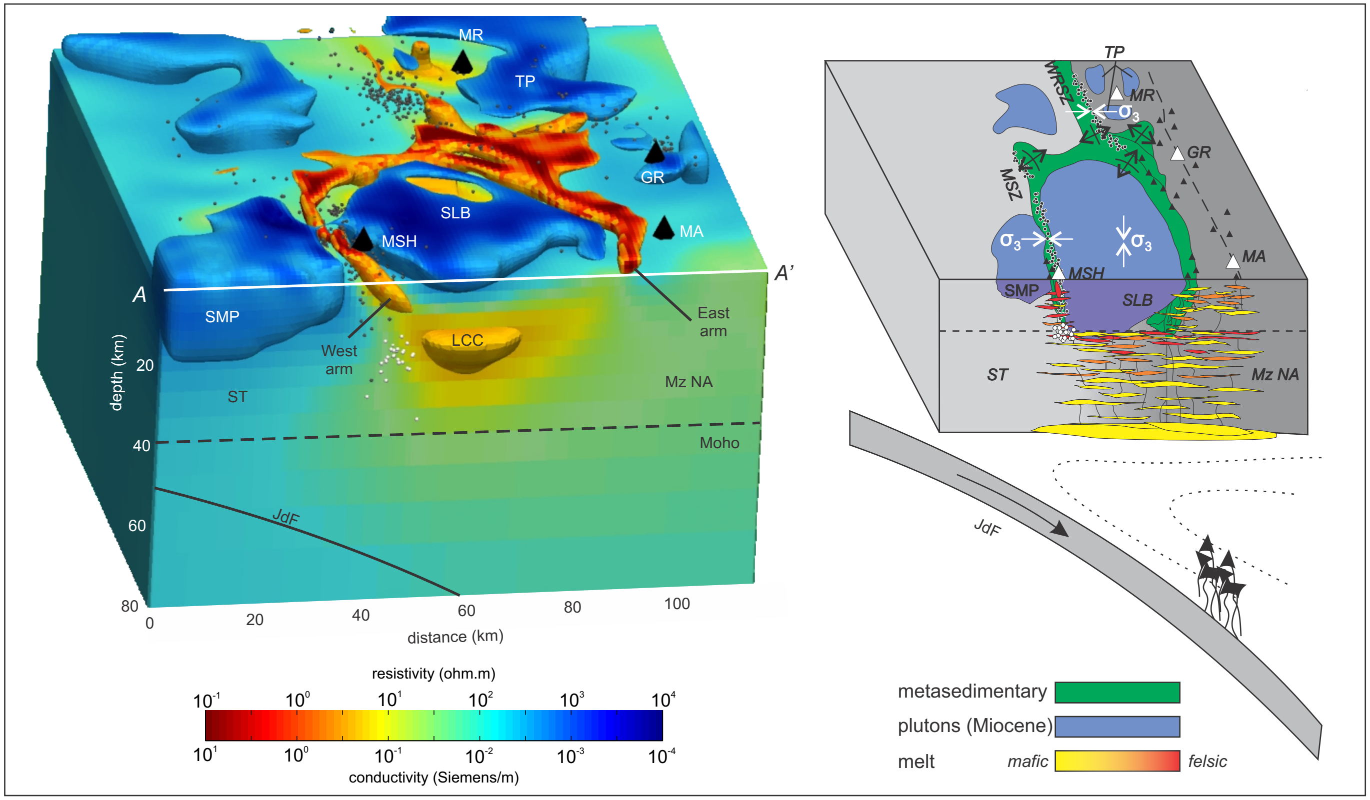

MR
TP
GR
SLB
MA
MSH
A
A'
SMP
East
arm
West
arm
LCC
depth (km)
20
ST
Mz NA
40
Moho
60
JdF
80
0
20
40
60
80
100
distance (km)
resistivity (ohm.m)
10^{-1} 10^{0} 10^{1} 10^{2} 10^{3} 10^{4}
10^{1} 10^{0} 10^{-1} 10^{-2} 10^{-3} 10^{-4}
conductivity (Siemens/m)
TP
WRSZ
MR
σ_3
GR
MSZ
σ_3
σ_3
MA
MSH
SMP
SLB
ST
Mz NA
JdF
metasedimentary
plutons (Miocene)
melt
mafic
felsic

Extended Data to accompany *‘Crustal inheritance and a top-down control on arc magmatism at Mount St. Helens’* by Bedrosian et al.

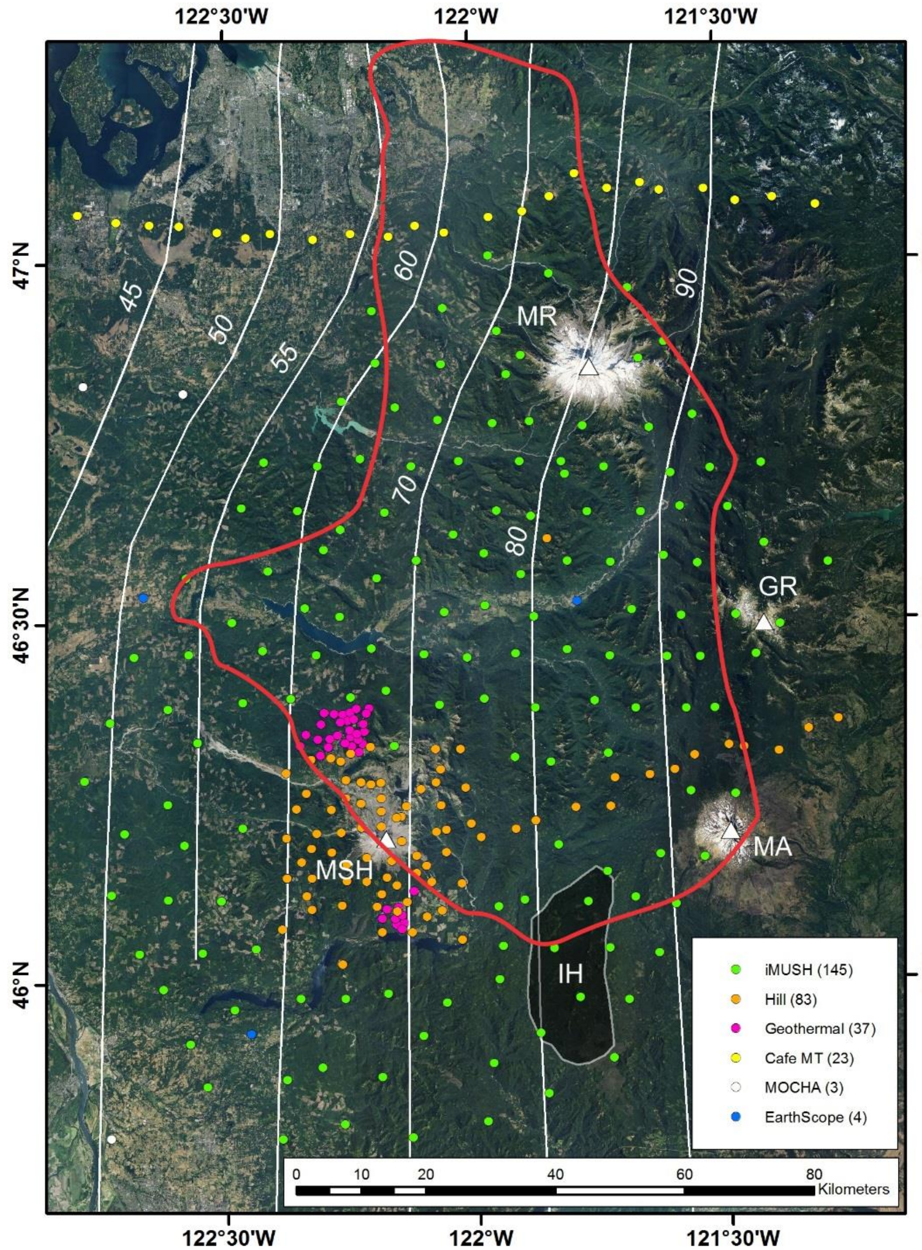

Extended Data Figure 1. Map of 295 magnetotelluric stations included within this study, color-coded by survey; number of stations included from each survey is in parentheses. Quaternary volcanoes shown as triangles. Goat Rocks (GR), Indian Heaven (IH), Mt. Adams (MA), Mt. Rainier (MR), Mount St. Helens (MSH). White solid lines denote drafted top-of-slab depth contours in kilometers[2]. Shaded region indicates extent of IH vent field. Red outline indicates approximate extend of Southern Washington Crustal Conductor as determined by previous studies[10].

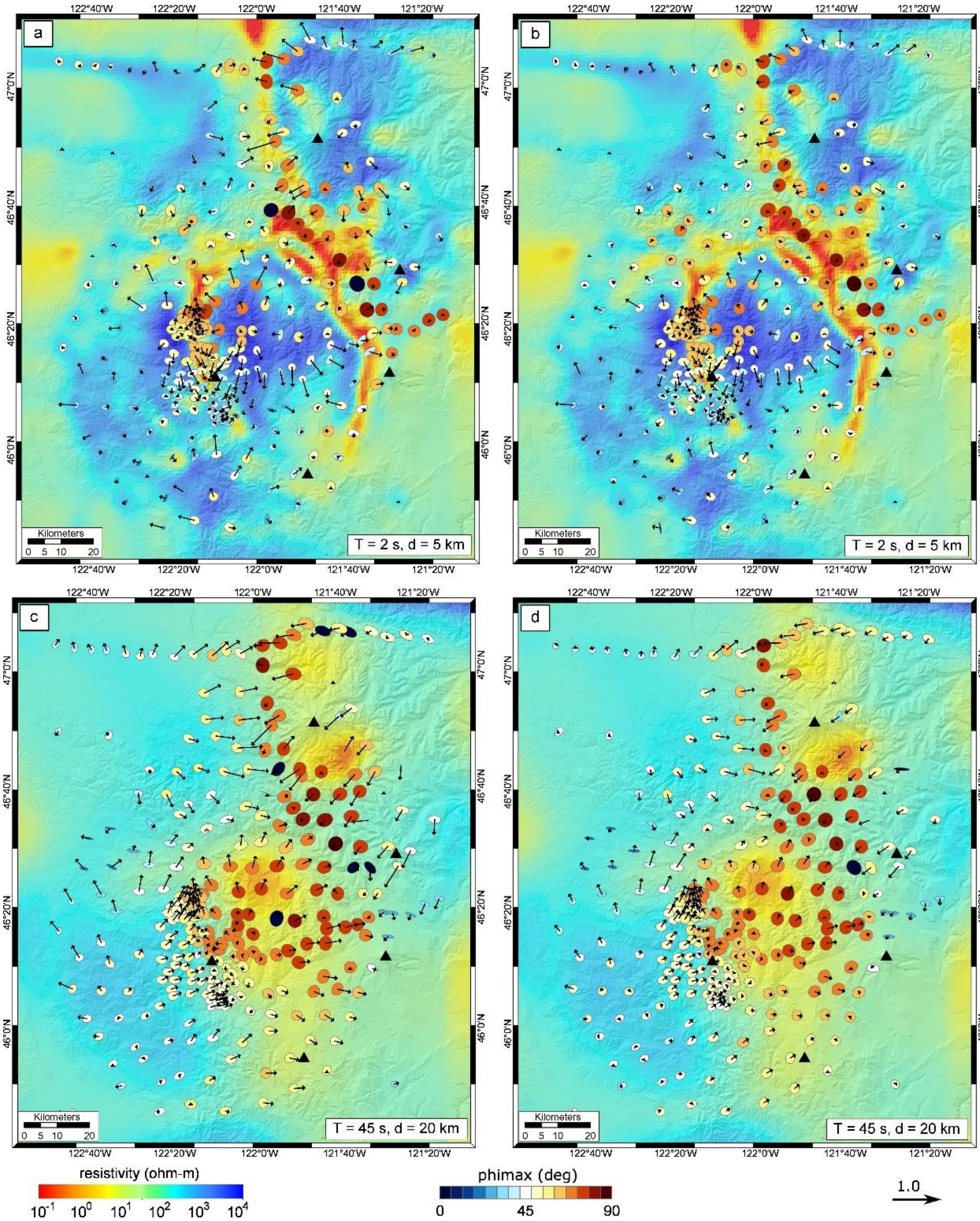

Extended Data Figure 2. (a) Measured and (b) modeled phase tensors and real induction vectors (Parkinson convention) at 2 s period overlain upon resistivity model at 5 km depth. Maximum phases approach 90º atop conductive belts and induction vectors reverse direction across them. Elevated maximum phase values in (c) measured and (d) modeled phase tensors at 45 s period reflect a broad conductive region in the lower crust parallel to the arc. Underlying image is the resistivity model at 20 km depth.

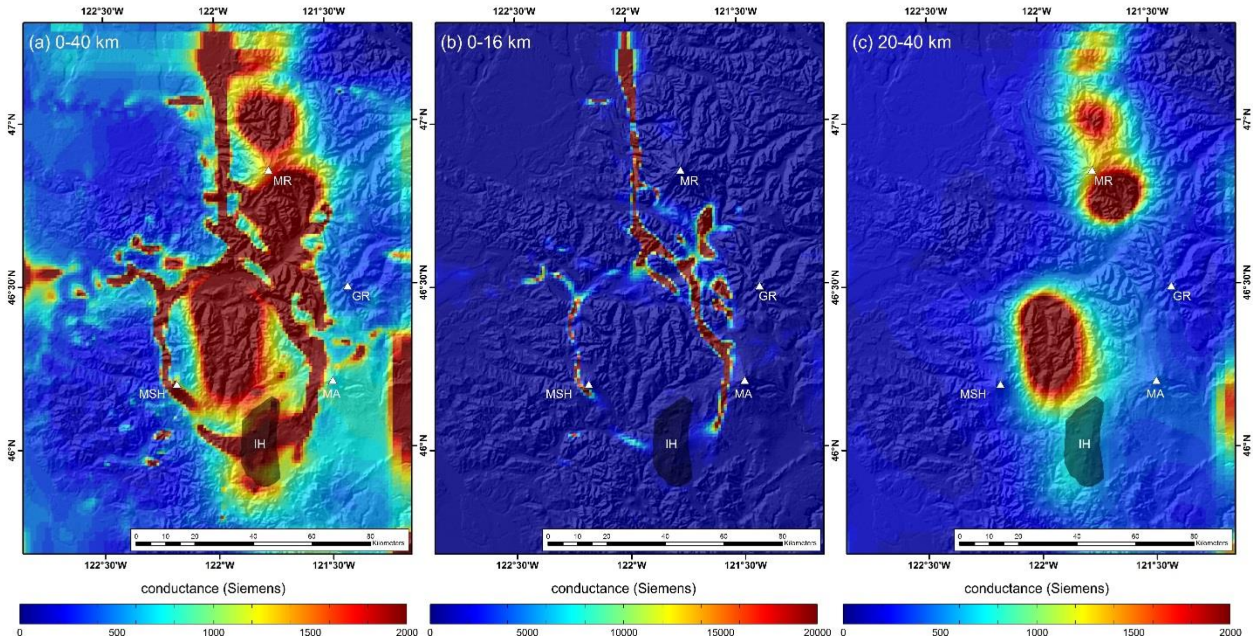

Extended Data Figure 3. Vertically-integrated model conductivity (conductance) for (a) the entire crustal column, (b) the upper crust, and (c) the lower crust. Crustal conductance can effectively be separated into upper- and lower-crustal contributions, the former of which is an order of magnitude larger than that of the latter. Abbreviations as in Figure 1.

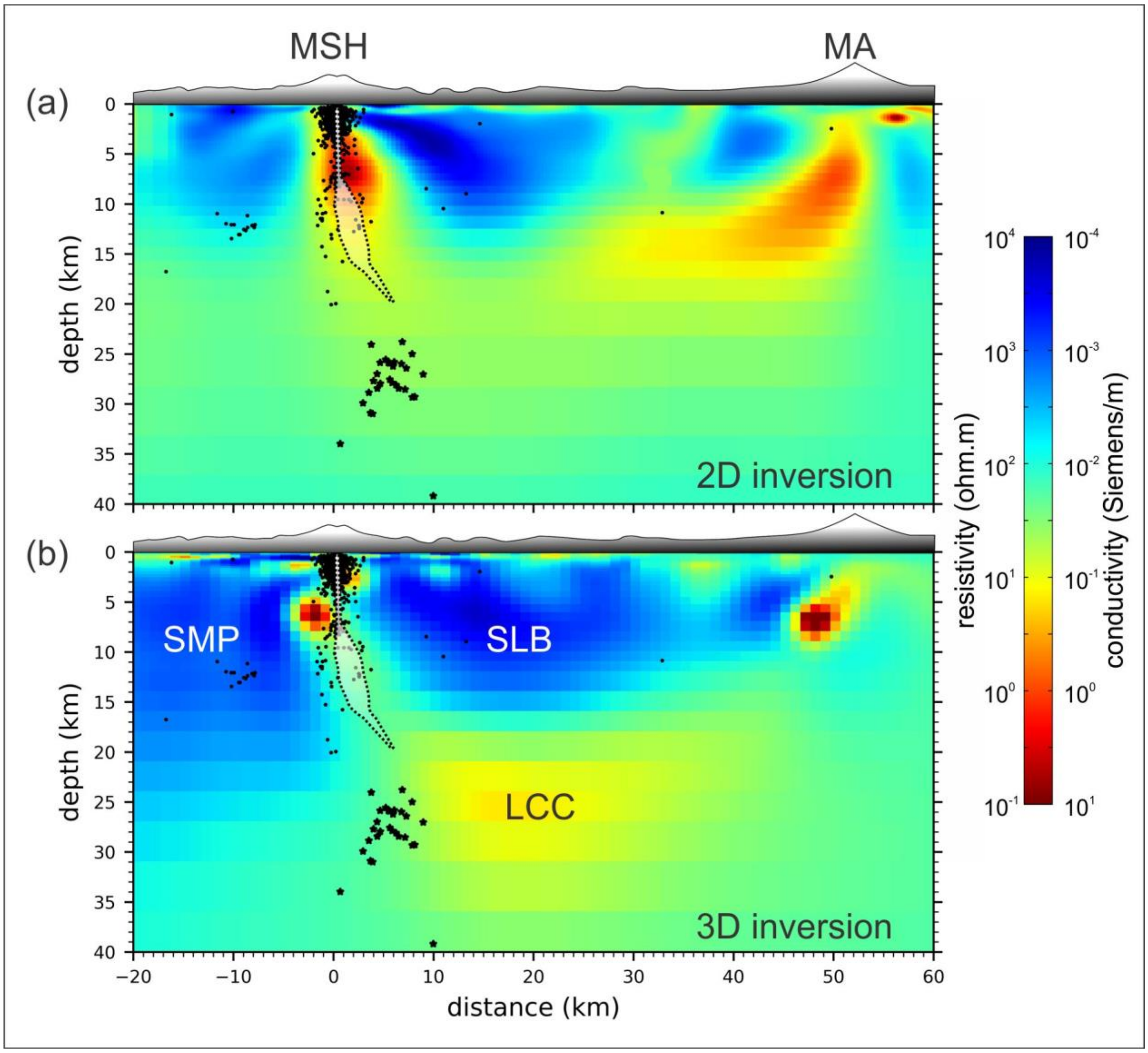

Extended Data Figure 4. Model comparison to past investigation of the SWCC. (a) Resistivity model obtained via 2D inversion[8] along a profile connecting MSH and MA. (b) Corresponding model slice through our 3D inversion model. Note similar model structure, however artificial connectivity between upper- and lower-crustal conductors in the 2D inversion model reflects the projection of off-profile conductance to depth. Black dots indicate seismicity greater than M=1 and within 1 km of the section. Black stars denote long-period earthquakes[30]. Dashed outline denotes the extent of the interpreted upper-crustal magma chamber beneath MSH[11].

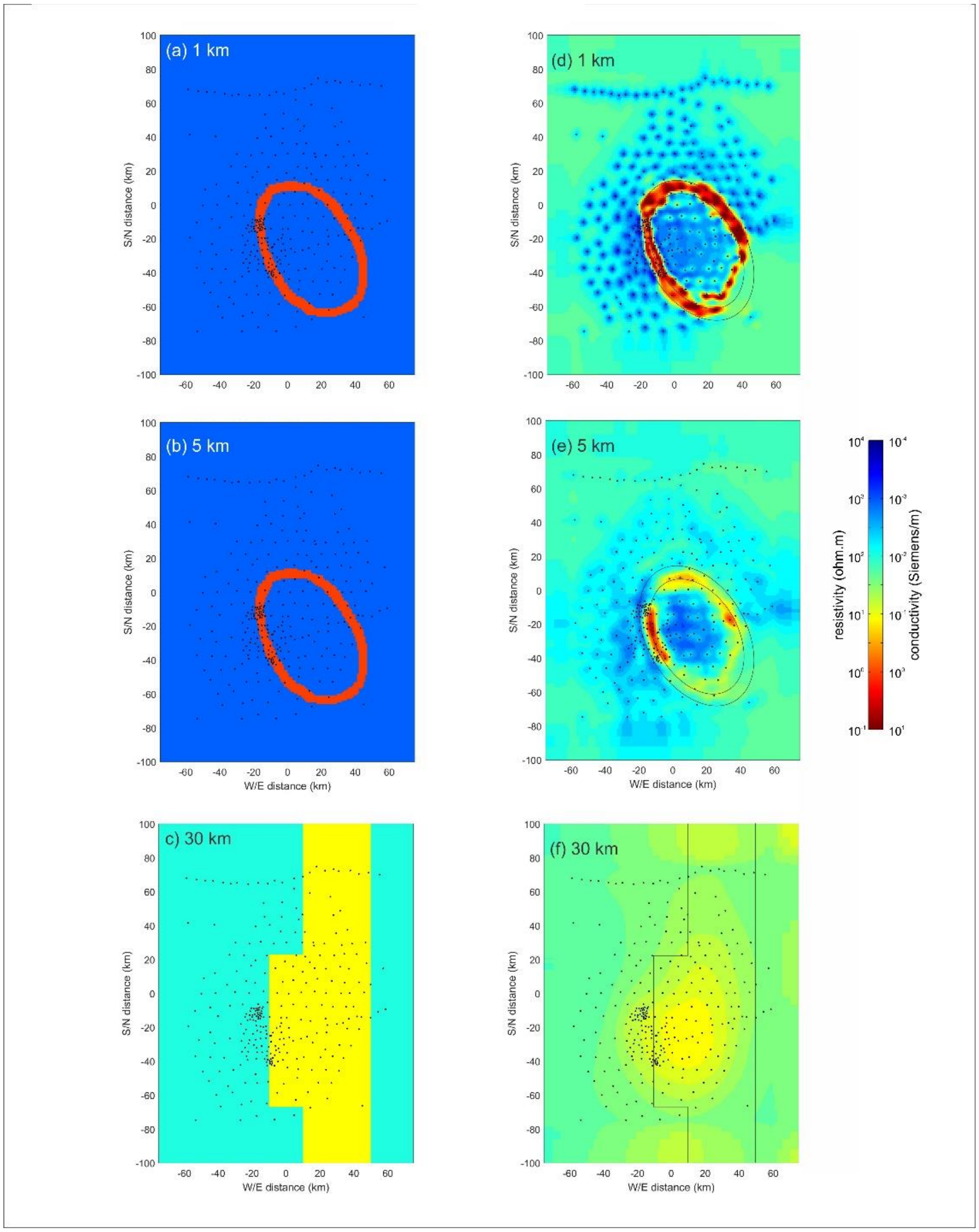

Extended Data Figure 5. Synthetic inversion study demonstrating the ability to resolve the UCC and LCC. Depth slices through the synthetic model at (a) 1 km, (b) 5 km, and (c) 30 km. Depth slice through the inverted resistivity model at (d) 1 km, (e), 5 km, and (f) 30 km. Approximate outlines of the conductors in the synthetic model are indicated by thin black lines.

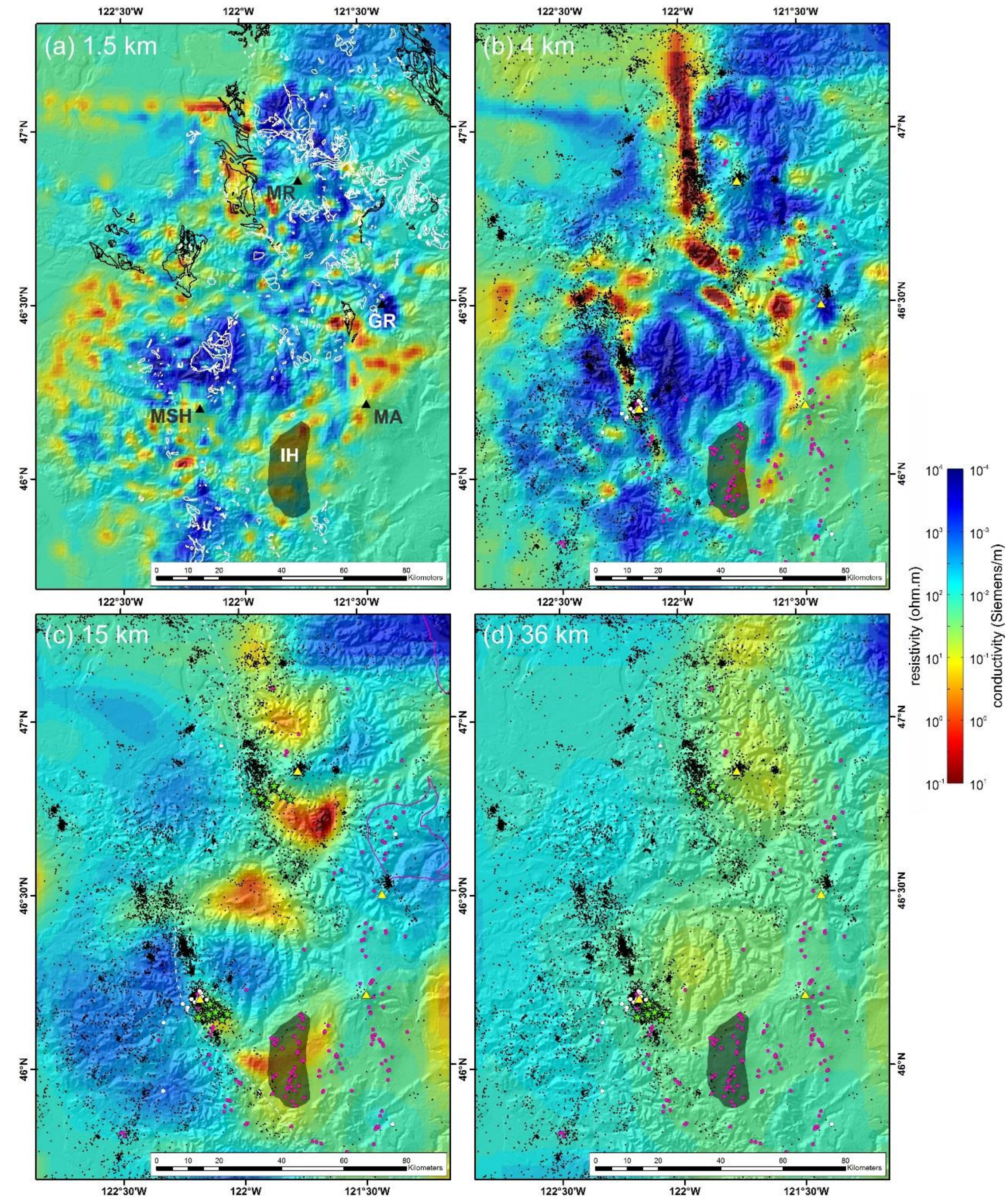

Extended Data Figure 6. Resistivity at (a) 1.5 km depth. Quaternary volcanoes shown as triangles. Mt. Adams (MA), Mount St. Helens (MSH), Mt. Rainier (MR), and Goat Rocks (GR). Grey shading indicates extent of Indian Heaven (IH) vent field. Outlines indicate the extent of Miocene intrusive rocks (white) and Eocene sedimentary rocks (black). (b) Resistivity at 4 km depth. Seismicity (black dots), Quaternary dacite vents (white circles), and other Quaternary vents (pink circles). (c) Resistivity at 15 km depth. Interpreted eastern edge of the Siletz terrane (white dashed line), exposed extent of Mesozoic rocks (pink outline), and deep long-period earthquakes[30] (green stars). (d) Resistivity at 36 km depth.

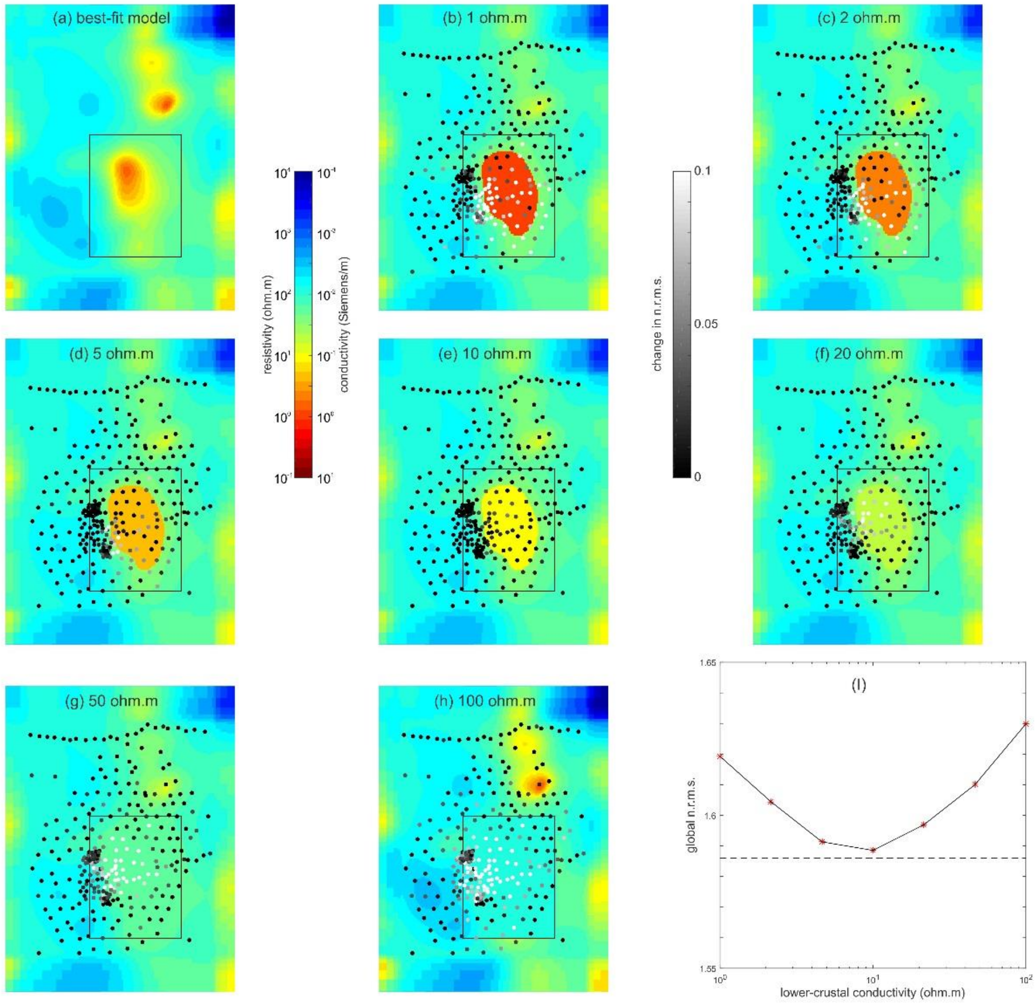

Extended Data Figure 7. Constraints on lower-crustal resistivity beneath the Spirit Lake Batholith. Rectangle denotes the region of modified lower-crustal resistivity (20 - 40 km depth) during subsequent modeling (a) Best-fit resistivity model at 25 km depth. Starting from this model, lower-crustal resistivity less than 30 Ω·m was replaced by (b) 1 Ω·m, (c) 2 Ω·m, (d) 5 Ω·m, (e) 10 Ω·m, (f) 20 Ω·m. Lower-crustal resistivity less than 50 and 100 Ω·m was replaced by (g) 50 Ω·m, (h) 100 Ω·m. Synthetic data responses are calculated for each model and the change in n.r.m.s. misfit (colored symbols) at each site calculated relative to the best-fit model. Global n.r.m.s. misfit vs lower-crustal resistivity (i) indicates that a lower-crustal resistivity of 10 Ω·m is most consistent with the measured data.

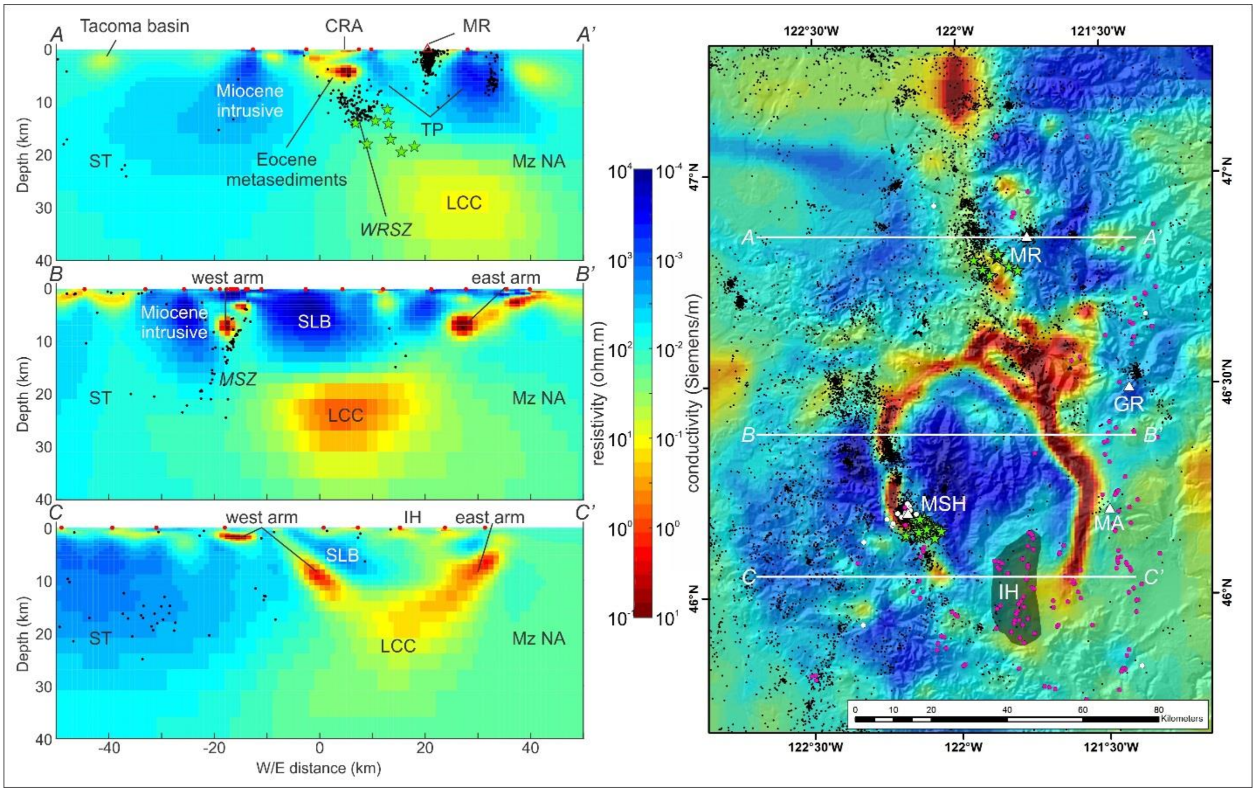

Extended Data Figure 8. Interpreted resistivity cross-sections through the study area. No vertical exaggeration. Stations within 2.5 km (red circles) of the section are projected at the surface. Black dots indicate seismicity greater than M=1 and within 1 km of the section. Quaternary dacite vents (white circles) and other Quaternary vents (pink circles). Stars denote deep long-period earthquakes[30]. Abbreviations as in Fig. 1 plus Carbon River anticline (CRA); lower-crustal conductor (LCC); Mesozoic North America (Mz NA); Mount St. Helens seismic zone (MSZ); Siletz terrane (ST); Spirit Lake batholith (SLB); Tatoosh pluton (TP); West Rainier seismic zone (WRSZ). Shaded region indicates extent of IH vent field.

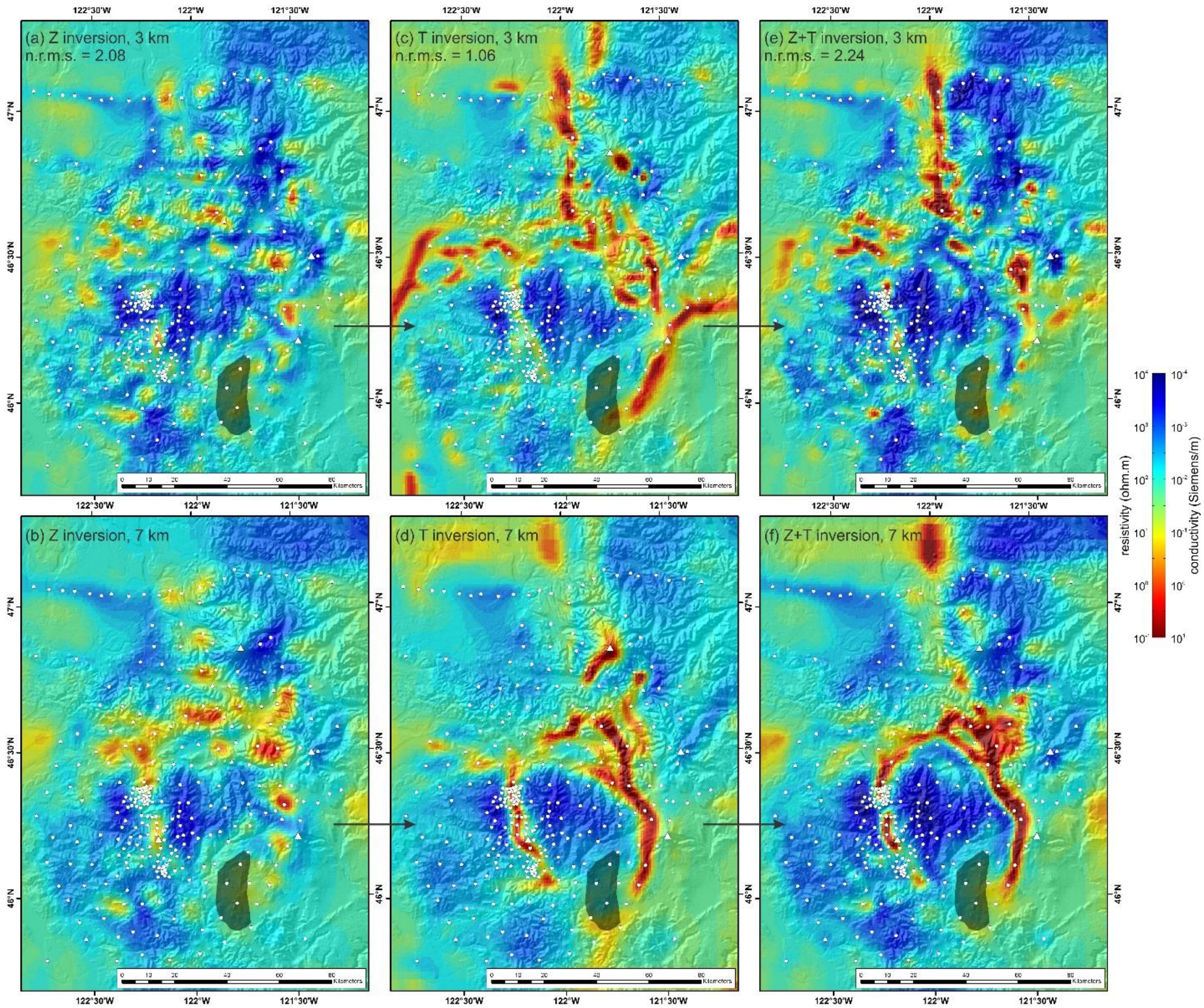

Extended Data Figure 9. Depth slices through the inversion model at each stage in the sequential inversion approach. An initial inversion (a, b) incorporated just impedance (Z) data subject to an error floor of 5% sqrt(|Zxy*Zyx|), using a model covariance of 0.3 applied twice, and a 100 Ω·m halfspace with ocean included as both the start and prior model. The resulting inverse model became the start model for subsequent inversion of tipper (T) data (c, d), subject to an absolute error floor of 0.03, with a revised model covariance of 0.2 applied twice and a homogeneous prior model. The result of the second inversion was used as the start model for a final inversion of both impedance and tipper (Z+T) data, with error floors of 4% sqrt(|Zxy*Zyx|) and 0.03, for impedance and tipper data, respectively.

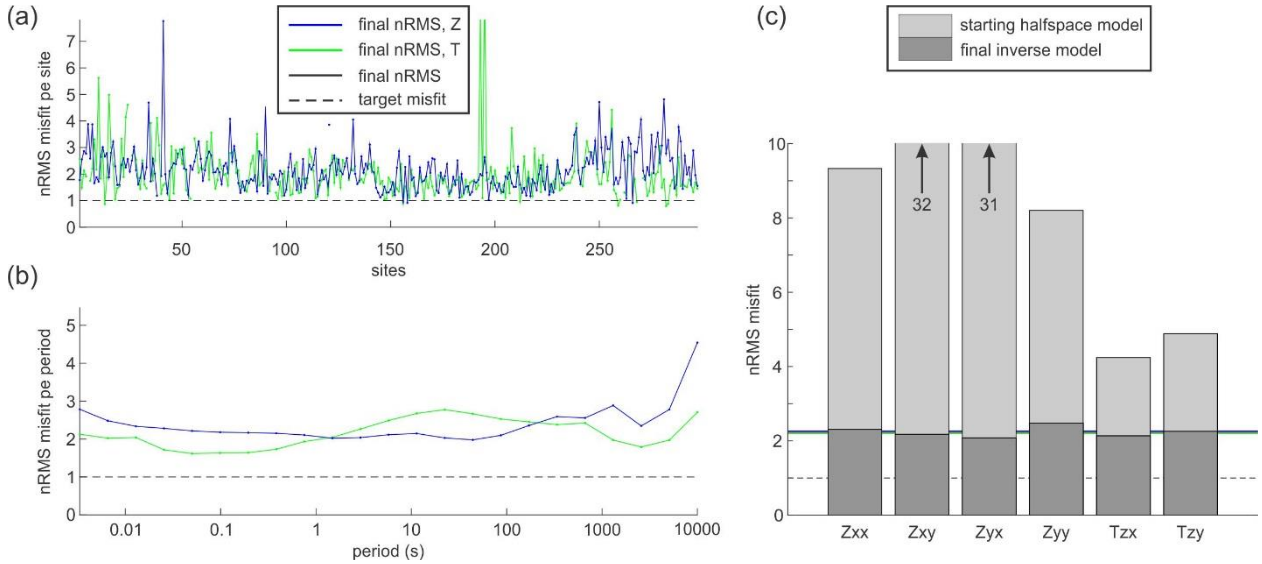

Extended Data Figure 10. Normalized root-mean-square (nRMS) data misfit broken down by (a) site, (b) period, and (c) component. Impedance (Z); vertical magnetic-field transfer function (T). Global nRMS for homogeneous start model and final inverse model equals 19.22 and 2.24, respectively.